LAWRENCE
LIVERMORE
NATIONAL
LABORATORY

LLNL-JRNL-698509

MEASUREMENT OF RUNAWAY ELECTRON ENERGYDISTRIBUTION FUNCTION DURING HIGH-Z GASINJECTION INTO RUNAWAY ELECTRON PLATEAUS

DIII-D

E. M. Hollmann, C. J. Lasnier

July 25, 2016

Physics of Plasmas

Disclaimer

LLNL-JRNL-698509

GA–A27969

MEASUREMENT OF RUNAWAY ELECTRON ENERGY DISTRIBUTION FUNCTION DURING HIGH-Z GAS INJECTION INTO RUNAWAY ELECTRON PLATEAUS DIII-D

by

E.M. HOLLMANN[1], P.B. PARKS[2], N. COMMAUX[3], N.W. EIDIETIS[2], R.A. MOYER[1], D. SHIRAKI[3], M.E. AUSTIN[4], C.J. LASNIER[5], C. PAZ-SOLDAN[2], AND D.L. RUDAKOV[1]

This is a preprint of an invited paper presented at the Fifty-sixth Annual Meeting of the Division of Plasma Physics, October 27-31, 2012 in New Orleans, Louisiana and to be submitted for publication in *Phys. Plasmas*.

[1]University of California, San Diego, La Jolla, California, USA
[2]General Atomics, P.O. Box 85608, San Diego, California, USA
[3]Oak Ridge National Laboratory, P.O. Box 2008, Oak Ridge, Tennessee, USA
[4]University of Texas, Austin, Austin, Texas, USA
[5]Lawrence Livermore National Laboratory, Livermore, California, USA

Work supported by
the U.S. Department of Energy
under DE-FG02-07ER54917, DESC0001961, DE-AC05-00OR22725, DE-FC02-04ER54698, DE-FG03-97ER54415, and DE-AC52-07NA27344

GENERAL ATOMICS PROJECT 30200
JANUARY 2015

GENERAL ATOMICS

Abstract

The evolution of the runaway electron (RE) energy distribution function f_ε during massive gas injection into centered post-disruption runaway electron plateaus has been reconstructed. Overall, f_ε is found to be much more skewed toward low energy than predicted by avalanche theory. The reconstructions also indicate that the RE pitch angle q is not uniform, but tends to be large at low energies and small q ~ 0.1 - 0.2 at high energies. Overall power loss from the RE plateau appears to be dominated by collisions with background free and bound electrons, leading to line radiation. However, the drag on the plasma current appears to be dominated by collisions with impurity ions in most cases. Synchrotron emission appears not to be significant for overall RE energy dissipation but may be important for limiting the peak RE energy.

1. Introduction

Runaway electron (RE) beams can form in tokamaks when large toroidal electric fields are present, typically during startup, strong radio-frequency current drive, discharge ramp down, or disruptions [1]. In extreme cases, post-disruption RE beams (sometimes called "RE plateaus" if sufficiently long-lived) can carry a significant (up to 80%) fraction of the initial pre-disruption plasma current, thus carrying significant energy [2]. RE plateaus can already damage plasma-facing components in present tokamaks [3] and the potential for damage will be even higher in the ITER tokamak due to the larger initial toroidal plasma current (15 MA) [4]. A multi-MA RE plateau-wall strike in ITER could lead to significant localized wall damage [5] and must therefore be avoided.

Present control system simulations indicate that position control of RE plateaus in ITER will only be achievable in certain optimum circumstances (good pre-disruption plasma centering, a high RE plateau current, and a low RE plateau current decay rate) [6]. Based on these simulations, it is presently assumed that position control will be lost if a RE plateau does form in ITER and that the RE plateau will drift vertically into the wall on a ~100 ms time scale.

Enhanced loss of REs using intentionally applied non-axisymmetric fields ("RMPs") is presently not considered to be a reliable RE mitigation method for ITER. Experiments toward avoiding RE plateau formation with RMPs have shown some positive results in JT-60U [7] and TEXTOR [8], but inconclusive results in DIII-D [9] or JET [10]. Simulations of the effect of RMPs on RE confinement in ITER indicate that REs near the edge of the plasma (minor radius $r/a > 0.8$) can be deconfined, but little effect is expected on the bulk of the REs [11].

In separate experiments in DIII-D and Tore-Supra, massive gas injection (MGI) of impurities into RE plateaus have demonstrated fairly rapid (<100 ms) dissipation of RE plateau current [12,13]. Higher-Z gases (Ne or Ar) were observed to dissipate RE plateau current faster than lower Z gas (He). These experiments suggest that MGI may be a useful method of RE plateau energy dissipation in ITER. However, for optimized implementation of MGI dissipation of RE plateaus in ITER, it will be important to understand the physics of RE plateau dissipation and the final wall strike. For example, too much high-Z material injection could lead to a very fast RE plateau current decay

which could accelerate the vertical loss rate and result in a higher current at the wall impact than with a moderate amount of high-Z material injection. On the other hand, a rapid motion of the RE plateau into the wall may be desirable to some degree, as this could reduce the time for conversion of RE plateau magnetic energy into kinetic energy during the wall strike [14].

Understanding the evolution of the RE energy distribution function is also crucial and is one of the goals of this paper. For example, if high-Z gas injection significantly increases loop voltage and "hardens" the energy distribution function, creating more high energy particles, this may increase the likelihood of deep wall damage and may be undesirable, even if the total RE energy and resulting surface melting is lowered.

In this work, the evolution of RE plateau energy is studied during MGI of noble gas (He, Ne, or Ar) into centered RE plateaus in the DIII-D tokamak [15]. It is found that the highest Z impurity (Ar) strongly increases the dissipation rate of the RE plateau energy. Ne is less effective and He the least effective. Overall, the dominant energy loss channel appears to be collisions with background cold plasma electrons, free and bound, leading to line radiation, with the exception of RE plateaus with very low high-Z impurity content, where synchrotron emission may become important. Traditionally, only collisions with background electrons have been considered for RE current dissipation [16], but measured RE current dissipation rates are higher than expected [12], motivating investigation of additional dissipation mechanisms. Here, it is demonstrated that ions may also serve an important role by pitch angle scattering of REs.

2. Experimental Setup

The experiments described here begin with steady inner wall limited, electron cyclotron heated (ECH), deuterium plasmas with toroidal magnetic field $B_\phi = 2.1$ T and plasma current $I_p = 1.2$ MA. These target plasmas are rapidly terminated with small cryogenic Ar pellet injection (diameter $D \approx 3.4$ mm, velocity $v \approx 200$ m/s, and volume $V \approx 15$ Torr - L $\approx 5 \times 10^{20}$ atoms) at time t = 1200 ms, forming a RE plateau. The plasma control system is programmed to hold the resulting RE plateau at a target current of $I_p = 275$ kA near the center of the vacuum vessel (usually until around 1800 ms when the ohmic coil runs out of V-s). These RE plateaus consist of mostly D^+ ions with low neutral content on center and of order 5-10% Ar^+ ions (left from the small Ar pellet). In

some shots, the impurity content of the RE plateau is then modified by massive gas injection (MGI) of He, Ne, or Ar gas (typically 50 – 100 Torr-L) at t = 1450 ms.

An overview of the main diagnostics used is shown in Fig. 1, with a top view in Fig. 1(a) and side views in Figs. 1(b-e). Background plasma line-integrated electron density is measured with CO_2 interferometers, shown in Fig. 1(c). Total plasma radiated power is measured with foil bolometers. Soft x-ray (SXR, 2 – 10 keV) emission is measured with AXUV photodiode-based arrays, shown in Fig. 1(d). Mid x-ray (MXR, 20 – 100 keV) emission is measured with a CdTe photodiode based array, shown in Fig. 1(e). Hard x-ray (HXR, 1 – 100 MeV) emission is measured with 20 BGO-based scintillation detectors arranged around the machine; typical poloidal arrangement is shown in Fig. 1(d). RE forward-beamed synchrotron emission is measured with tangentially viewing visible and IR cameras. The visible camera is bandpass filtered to an Ar line-free region at 790 nm with 10 nm FWHM, while the IR camera is left unfiltered and is sensitive from 3-5 mm. Background plasma composition and temperature are estimated with tangentially viewing UV and visible survey spectrometers. The observed spectra are dominated by line emission in the visible range and radiative recombination continua in the UV range; in this article, we simply use "line radiation" to refer to either individual lines or recombination continua.

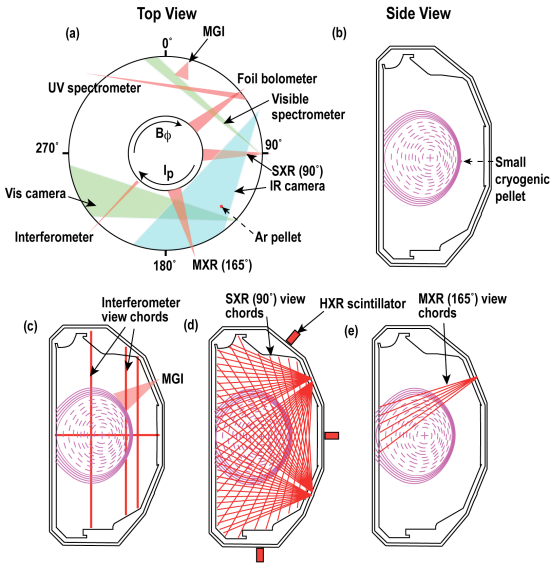

Fig. 1. Overview of main diagnostics used showing (a) top view, (b) side view with Ar pellet injector, (c) side view with MGI port and interferometer view chords, (d) side view with SXR view chords, and (e) side view with MXR view chords.

3. Data Analysis

The focus of the present work is reconstruction of the RE energy distribution function f_ε during MGI into the RE plateau. Here, we use a top-hat radial profile assumption, i.e. f_ε is taken to be constant out to the RE plateau minor radius a_{RE} and then 0 after that. In

reality, the RE plateau has radial structure: indications of this are shown in Fig. 2. However, the line-integrated nature and limited number of view chords of many of the diagnostics would make accurate reconstruction of $f_\varepsilon(r)$ extremely difficult. For an estimate of the RE beam minor radius a_{RE}, the midplane profile of the tomographically reconstructed SXR emissivity, Fig. 2(b), is used, typically obtaining $a_{RE} \approx 0.2$ m, consistent with separate estimates of the width of the bulk of the RE plateau current channel using RE plateaus driven into the wall [12].

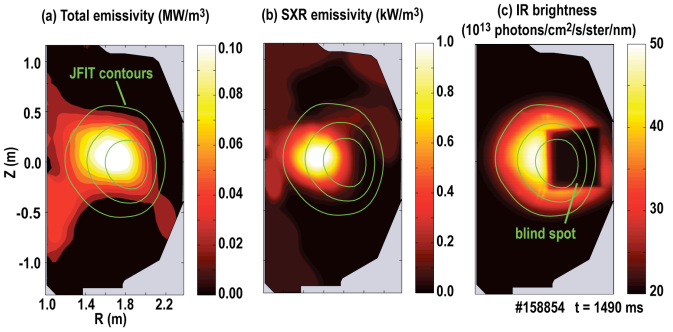

Fig. 2. Examples of measurements of the radial structure of the RE plateau showing (a) tomographic reconstruction of total emissivity from foil bolometer arrays, (b) tomographic reconstruction of SXR emissivity from SXR arrays, and (c) IR synchrotron brightness from tangentially viewing IR camera. Green curves are estimates of magnetic flux contours from current filament (JFIT) reconstructions [21].

In order to interpret the plasma x-ray emission, which comes dominantly from bremsstrahlung from RE-impurity ion collisions, the impurity density of the plasma needs to be known. The Ar-I, Ar-II, and Ar-III densities of the plasma are estimated by assuming Saha equilibrium between Ar and Ar^+ and performing Saha-Boltzmann fits to Ar-I and Ar-II upper state population densities measured with the visible survey spectrometer to obtain Ar^+ and Ar^{2+} densities. An example is shown in Fig. 3(a) which shows a Saha-Boltzmann fit to Ar-II line brightnesses. It can be seen that the plot of $\log(n_k/g_k)$,

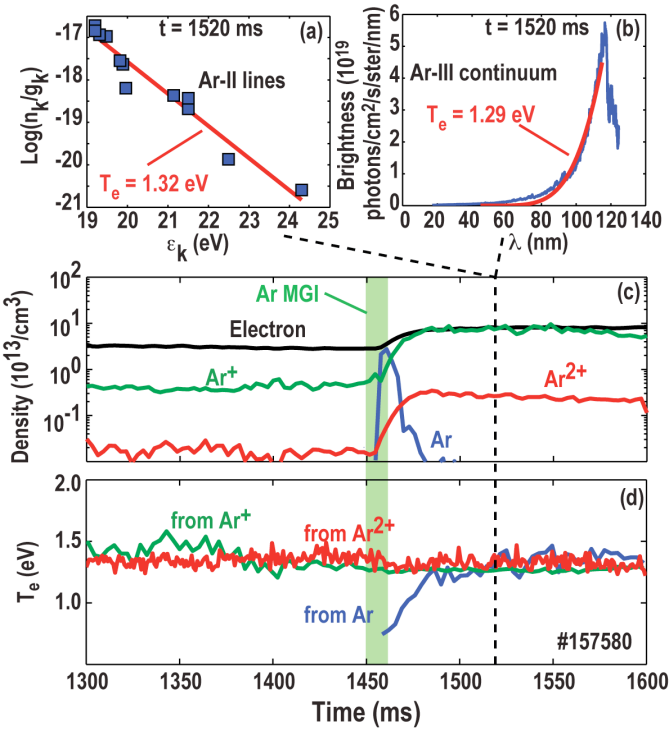

Fig. 3. Analysis of argon densities in RE plateau showing (a) Saha-Boltzmann fit to Ar-II upper state densities, (b) fit to Ar-III free-bound radiative recombination continuum, (c) time sequence of electron and argon ion densities, and (d) time sequence of electron temperatures at various argon charge states.

the logarithm of upper state density divided by statistical weight, is linear with upper state energy ε_k, consistent with the upper states being in pLTE (partial local thermal equilibrium) and justifying the use of Saha-Boltzmann analysis. The analysis requires a profile-averaged cold free electron density n_e; this is estimated from the four interferometer view chords. For the purposes of achieving the average n_e over the RE beam diameter, the data is first fit assuming that the radial profile $n_e(r)$ is an inverted parabola inside the RE beam $r < a_{RE}$ and constant at larger radii $r > a_{RE}$. This shape was shown to be a reasonable approximation in shots where it was possible to perform tomographic inversions of interferometer data with rapidly vertically scanned RE plateaus [12].

Figure 3(c) shows the time evolution of argon charge states following Ar MGI into a RE plateau, estimated with visible spectroscopy as discussed above. It can be seen that the main impurity is initially about 10% Ar^+. Following Ar MGI, this increases rapidly (within about 10 ms) to nearly 100% Ar^+. The Ar^{2+} density is typically more than $10\times$ smaller than Ar^+. The free-bound continuum from radiative recombination of Ar^{2+} into Ar^+ can be seen clearly in the UV range, Fig. 3(b), supporting the presence of some Ar^{2+}, and giving a measure of the cold electron temperature T_e at the Ar^{2+} location. The neutral Ar density is typically quite small in the RE beam except during Ar MGI, when it briefly becomes significant. The cold electron temperature T_e at the Ar neutral location Fig. 3(d) can be seen to approach T_e at Ar^+ and Ar^{2+} over time. This is consistent with Ar diffusing in to the RE plateau, heating, and mostly ionizing into Ar^+.

The energy distribution function of REs in the plateau covers a broad energy range from the keV to the MeV level. No single DIII-D diagnostic is able to measure this broad energy range, so f_ε is reconstructed by fitting to multiple diagnostics simultaneously. Relative sensitivities of different DIII-D diagnostics to RE energy are shown in Fig. 4(a). At the low energy (keV) end, SXR emission is the most sensitive diagnostic, while at the high energy (MeV) end, visible synchrotron emission is the most sensitive, but only measures REs with energies above 30 MeV or so. Total radiated power (line emission) is sensitive to a fairly wide range of energies, as is electron cyclotron emission (ECE). The ECE spectrum is measured with a Michelson interferometer in DIII-D but is not used as a constraint in the present analysis, as it is found to be extremely sensitive to the RE and cold electron radial profiles and is therefore not well suited for the present 0D analysis. Figure 4(b) shows the normalized sensitivities (except ECE) as a function of energy weighted with a typical energy distribution function at a single time step. This

demonstrates that many of the diagnostic signal levels (after convolution with the energy distribution function) are expected to come from a fairly narrow range of energies.

A sample reconstructed energy distribution function f_ε at one time step is shown by the black curve in Fig. 5(a). Figure 5(c) shows the sine of the reconstructed RE pitch angle θ. We assume here for simplicity that REs at a single energy have a single pitch angle θ. Both f_ε and θ are assumed to be a slowly varying functions of energy e and are therefore represented in the optimization routine by a small number of knot points, with interpolation between knot points performed with a smoothed spline. The free parameters in the optimization routine are therefore the number of knot points, the degree of smoothing used on the solution, and the relative weights of the different diagnostic errors on the total error to be minimized. To reduce possible biases in f_ε due to knot point selection, two different energy grids were chosen here: one with 9 knot points going logarithmically from 2 keV to 60 MeV, and one with 9 knot points going logarithmically from 5 keV to 80 MeV, with the final f_ε given by the average of the two f_ε solutions. Because the actual expected error (residual) of each diagnostic is poorly known, the total error was defined here simply as the sum of all the fractional errors between the measured and reconstructed signal levels. The shaded regions show upper and lower bounds in f_ε and θ estimated by moving knot points and testing the response of the total error. The relative large uncertainty in f_ε in the 0.1 – 1 MeV range corresponds to the lack of constraining diagnostic coverage over this energy range, as can be seen in Fig. 4(b). Over, this energy range, the only constraints are the MXR diagnostic, and to a lesser degree, total radiated power and plasma current, resulting in large uncertainty in f_ε. Figures 5(b, d) show moments of the distribution function: the energy moment $f_\varepsilon \varepsilon d\varepsilon$ is plotted in Fig. 5(b) and the current moment $f_\varepsilon v_\parallel d\varepsilon$ is plotted in Fig. 5(c). It can be seen that current tends to be carried by electrons in the 1 – 10 MeV range. The data points in Fig. 5(a) are simplified

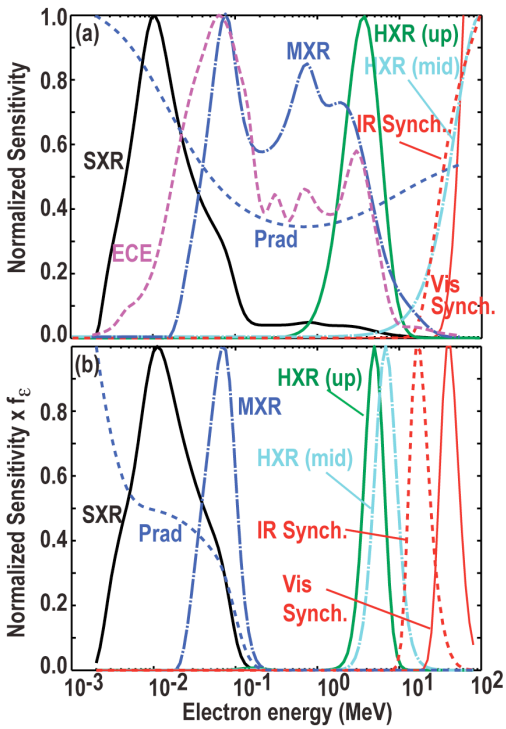

Fig. 4. (a) Relative sensitivities of different DIII-D diagnostics to RE energy and (b) relative sensitivities (except ECE) weighted by a typical energy distribution function, shown in Fig. 5(a).

single energy approximations to f_ε; i.e. it assumed that the signal to each diagnostic comes only from electrons in the energy range corresponding to the FWHM of the weighted sensitivity curves of Fig. 4(b) and that f_ε is constant over this energy range. This serves as a rough cross check of the more rigorous smoothed spline reconstruction, giving discrete values of f_ε which are reasonably close to the smoothed spline f_ε.

The blue dot-dash curve in Fig. 5(a) is the distribution function predicted by avalanche theory $f_\varepsilon \sim \exp(-p/\bar{p})$ where p is electron momentum normalized by $m_e c$, $\bar{p} \approx 46$ for drag on REs dominated by bound Ar electrons and free electrons, and the normalization to f_ε is provided by the total plasma current [16]. It can be seen that the reconstructed distribution function is significantly skewed toward low energies relative to the avalanche theory prediction. The green dashed lines show a two power-law fit to f_ε to provide a rough characterization of the shape of the distribution function. At low energies, a very slow power law decay $f_\varepsilon \propto \varepsilon^{-0.25}$ is shown, while at high energies, a very strong decay $f_\varepsilon \propto \varepsilon^{-6}$ is shown.

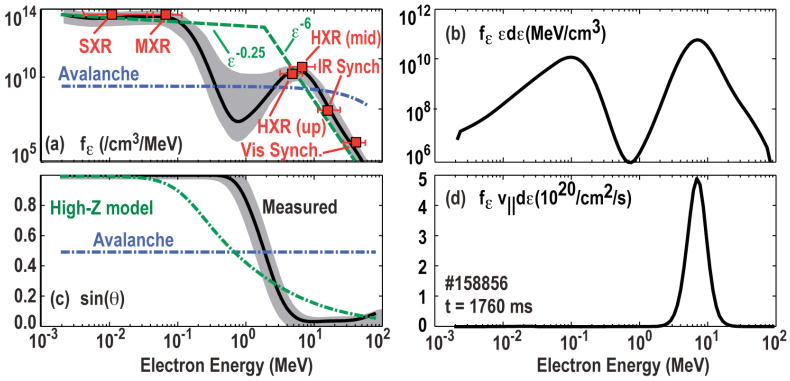

Fig. 5. Examples of reconstructions of (a) RE energy distribution function f_ε (solid curve); (b) energy moment of measured energy distribution function; (c) RE pitch angle q (black curves); and (d) current moment of measured energy distribution function.

Figure 5(c) indicates that the pitch angle is very isotropic at low energies and then becomes more directional at high energies. This contrasts with avalanche theory, where an isotropic half-Maxwellian is assumed, giving sin(θ)~ ½. The measured pitch angle decrease with energy is qualitatively consistent with a quasi-steady solution of the relativistic kinetic equation in the large Z case, where $Z >> \hat{E} \sim 1$ is expected during the slowly evolving plateau phase. Physically, the faster processes, namely collisional pitch-angle isotropization and flattening of the pitch angle due to the torque acting on the electron by the electric field, should be in balance at all moments. This balance leads to a distribution function of the form $f(\gamma,\mu) \propto g(\gamma)\exp[\mu\lambda(\gamma)]$, where $\mu = \cos\theta$. Then the mean value of μ will be,

$$\langle\mu\rangle = \coth(\lambda) - \lambda^{-1} \quad , \tag{1}$$

where

$$\lambda(\gamma) = \frac{2E}{[1+\langle Z\rangle]}\left(\frac{\gamma^2-1}{\gamma}\right) \quad , \tag{2}$$

γ is the standard Lorentz factor, and $\hat{E} \equiv E/E_{crit}$ is the normalized parallel electric field with E_{crit} being the critical electric field $E_{crit} = \left(e^3/4\pi\varepsilon_0^2 m_e c^2\right)\sum_j n_{e,j} \ln\Lambda_{ee,j}$. The mean charge state in Eq. (2) does not correspond to the standard mean charge state Z_{eff} for low energy Coulomb collisions, but is the effective nuclear charge seen by relativistic electrons [17]:

$$\langle Z\rangle \equiv \sum_k n_k Z_k^2 \ln\Lambda_{ei,k} / \sum_j n_{e,j} \ln\Lambda_{ee,j} \quad , \tag{3}$$

where n_k, Z_k are the density and nuclear charge of species *k* and $\ln\Lambda_{ei,k}$ is the electron-ion Coulomb logarithms for relativistic electron collisions with nucleus Z_k. The sum $\sum_j$ is over all electron populations (e.g. bound Ar electrons, bound Ne electrons, or free electrons) and $\ln\Lambda_{ee,j}$ are the corresponding electron-electron Coulomb logarithms. For the example shown in Fig. 5, $\langle Z\rangle \approx 5$ and $\hat{E} \approx 11$. The green dot-dash curve in Fig. 5(c) shows the prediction of Eq. (1) for pitch angle as a function of RE energy. For the purposes of comparison with experiment, we approximate $\sin(\theta) \approx \sqrt{1-\langle\mu\rangle^2}$ with $\langle\mu\rangle$ given by Eq. (1). It can be seen that the steady-state prediction captures the observed trend of dropping θ at high energies.

The curves of Fig. 5 correspond to a single optimization at one time step. Examples of the quality of the fits to the raw data as a function of time are shown in Fig. 6. Time traces are shown for RE-profile-averaged quantities: SXR emissivity, MXR emissivity, HXR scintillation signal (midplane and upper detectors), visible synchrotron brightness, and IR synchrotron brightness. Also used as constraints in the reconstructions are: total plasma current (assuming all current is carried by REs) and total radiated power. In the case of total radiated power, it is assumed that power deposited by RE stopping on plasma ions and cold electrons (using stopping power curves for relativistic electrons) all goes into radiation, i.e. it is assumed that radial transport loss of power is small. Experiments indicate that this is a reasonable assumption for well-centered RE plateaus but breaks down if the RE plateau moves into the wall [12]. Overall, it can be seen that the fits to the raw data are reasonably good, typically within a factor of 2-3. This level of uncertainty is reasonable for most of the diagnostics used here, with the exception of

plasma current, which has a fit error reaching up to 50% in Fig. 6(g): this is probably larger than the uncertainty in the I_p measurement, although this minor inconsistency in the present optimization routine not expected to affect the results shown here. In contrast, it can be seen that the avalanche distribution function does a poor job of fitting some of the diagnostics. The disagreement is especially strong at the energy extremes, with SXR fits and synchrotron brightness fits being off by 3 orders of magnitude.

4. Results

The reconstructions of the energy distribution function f_ε as a function of time allow calculation of the evolution of RE plateau kinetic energy W_{kin} during MGI into the RE plateau. This is shown in Fig. 7, where examples are shown of the evolution of W_{kin} vs. time following (b) He MGI, (d) Ne MGI, and (f) Ar MGI. For comparison, the magnetic energy W_{mag} is also included. Here, we define W_{mag} as the magnetic energy stored inside the vacuum vessel, estimated from the magnetic filament reconstructions (JFIT) [18]. Although the magnetic energy external to the conducting wall is typically of similar magnitude, the internal magnetic energy is expected to be most important in ITER, with external magnetic energy not affecting the dynamics of RE-wall strikes [14]. For each experiment, the loop voltage V_{loop} is plotted as well. This is important because the plasma control system is attempting to maintain constant current and will therefore raise V_{loop} if

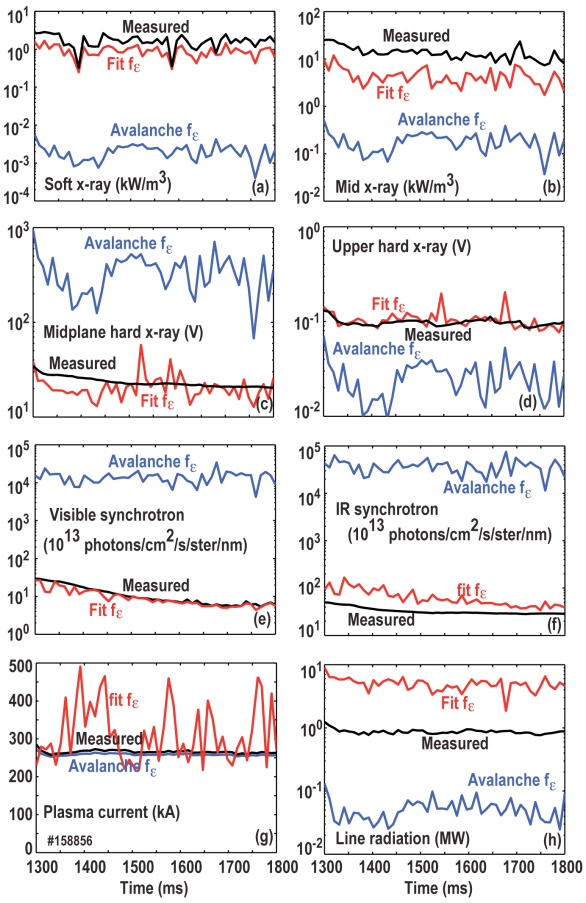

Fig. 6. Quality of fits to raw data (black) vs. time showing reconstructed distribution function fit (red) and avalanche distribution function fit (blue). Profile-averaged data shown is: (a) SXR emissivity, (b) MXR emissivity, (c) midplane HXR, (d) upper HXR, (e) visible (790 nm) synchrotron brightness, (f) IR (3-5 mm) synchrotron brightness, (g) plasma current, and (h) total radiated power (line radiation).

current dissipation increases. Both external (from a resistive loop) and internal (from JFIT reconstructions) loop voltages are plotted. These are expected to be similar in steady-state, but internal loop voltage is expected to be more accurate during transients. It can be seen that the behavior of the RE plateau is quite different for different species MGI. In the case of He MGI, the loop voltage drops slightly, indicating a decrease in current dissipation; this is thought to be due to Ar from the initial pellet being purged from the plasma. In the case of Ne MGI, there is a significant rise in V_{loop} (to about 10 V), a drop in W_{mag} and a rise in W_{kin}. Finally, in the case of Ar MGI, there is a very large rise in V_{loop} (to about 15 V) an extremely rapid drop in W_{kin} and a somewhat slower drop in W_{mag}. This demonstrates extremely different trends in energy dissipation with different MGI species and also demonstrates that W_{mag} and W_{kin} energy dissipation are not equivalent in these experiments, i.e. one can be dissipated more quickly than the other.

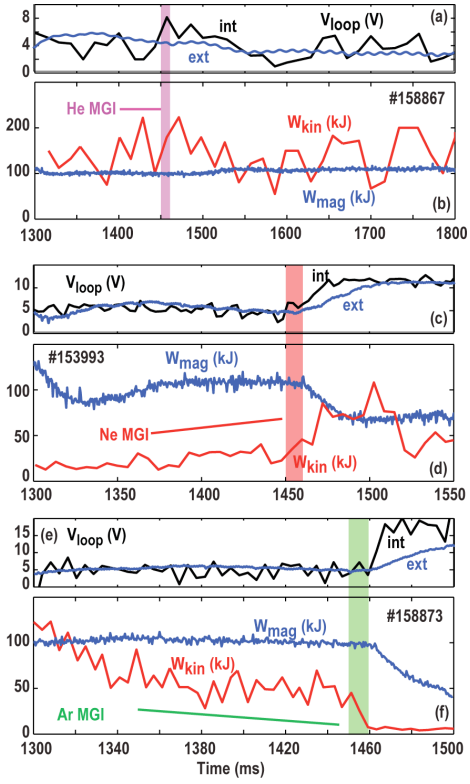

Fig. 7. Time evolution of W_{kin} and W_{mag} following (b) He MGI, (d) Ne MGI, and (f) Ar MGI; as well as (a), (c), and (e) V_{loop} for each case.

Power balance indicates that the dominant energy dissipation mechanism is line radiation for RE plateaus with significant Ar content. This is shown in Fig. 8, where ohmic input power ($V_{loop}I_p$) is plotted as black points as a function of mean plasma charge state $\langle Z \rangle$. Each data point in Fig. 8 corresponds to a 50 ms bin during a centered RE plateau. Line radiation power P_{rad} measured with the foil bolometer array is shown with light blue triangles. Additionally, synchrotron power emitted is shown with red points and x-ray bremsstrahlung power with green points. The last two quantities are calculated from the reconstructed f_ε. Power radiated in the microwave range via electron cyclotron emission is also measured, but is typically an order of magnitude below x-ray bremsstrahlung power and is therefore left off Fig. 8. Colored bands indicate the approximate estimated range of uncertainty in the data. It can be seen that input power and P_{rad} tend to be in reasonable agreement except for at very low $\langle Z \rangle$, shots corresponding to He MGI. In these shots, there is an apparent mismatch in input and output power, possibly due to the

synchrotron power being underestimated. The synchrotron power is extremely sensitive to f_ε and θ and therefore has a fairly large uncertainty. These shots are all fairly well centered, so radial transport loss of power is expected to be small compared with input power.

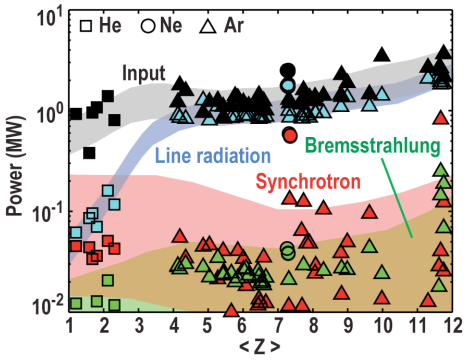

Fig. 8. RE plateau power balance as a function of mean charge state $\langle Z \rangle$ showing input power, line radiation power loss, synchrotron power loss, and x-ray bremsstrahlung power loss.

Previous experiments on RE plateaus in DIII-D without additional MGI, i.e. RE plateaus with ~5-10% Ar content, showed a current decay rate significantly faster than predicted by avalanche theory [19]. This is also observed in the present experiments with varying impurity content. This is shown in Fig. 9, where current damping rate ν_I is plotted with black points as a function of $\langle Z \rangle$. Here, we define the current damping rate as:

$$\nu_I \equiv eE/m_e c\bar{p} - \dot{I}_p/I_p \quad , \tag{4}$$

where E is the toroidal electric field and $\dot{I}_p/I_p$ is the measured plasma current growth rate. According to avalanche theory, which includes only electron drag, we expect $\nu_I \equiv eE_{crit}/m_e c\bar{p}$; these expected values are shown as light blue points in Fig. 9. It can be seen that the measured current damping rate is typically close to 10× higher than predicted from electron collisions only, except at the highest and lowest values of $\langle Z \rangle$.

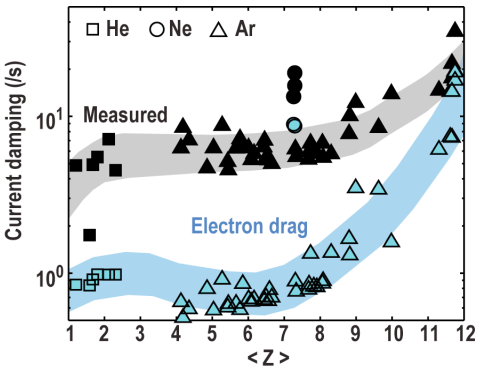

Fig. 9. Current damping rate ν_I measured as a function of mean ion charge $\langle Z \rangle$.

It is possible that the disagreement between the measured and predicted current damping rate seen in Fig. 9 is due to the exclusion of ion collisions in the theory. The importance of ion collisions for pitch angle scattering in these experiments is supported by Fig. 10, where the measured pitch angle scattering rate is plotted with black points as a function of $\langle Z \rangle$. Based on the equation of motion for a single relativistic electron [20], we define the measured pitch angle scattering rate as:

$$\nu_\theta \equiv d\theta/dt + \frac{eE\sin\theta}{m_e cp} \quad , \tag{5}$$

where $d\theta/dt$ is the rate of change of pitch angle obtained from data such as Fig. 5(c) and the electric field term reflects the expected reduction of pitch angle by the parallel electric field. The dominant terms increasing the mean pitch angle are expected to be electron and ion collisions: $\nu_{\theta,e} = \frac{eE_{crit}\gamma \sin\theta\cos\theta}{m_e c p^3}$ and $\nu_{\theta,i} = \langle Z\rangle \nu_{\theta,e}$ [20]. The emission of synchrotron radiation is also expected to increase pitch angle, as roughly $\nu_{\theta,R} = \frac{p\sin\theta}{\tau_R \gamma^2}$, where $\tau_R \equiv \frac{3}{2}\frac{\rho_{ec}^2}{r_e c}$ is the characteristic synchrotron emission timescale, with $\rho_{ec} = eB/m_e c$ and $r_e = e^2/\left(4\pi\varepsilon_0 m_e c^2\right)$ [21]. Because θ varies with energy, all terms are averaged over differential current to arrive at average pitch angle scattering rates weighted to those electrons which carry the most current, e.g. $\langle \nu_\theta \rangle_\parallel \equiv \int \nu_\theta(\varepsilon) f_\varepsilon(\varepsilon) v_\parallel d\varepsilon / \int f_\varepsilon(\varepsilon) v_\parallel d\varepsilon$. It can be seen that the measured $\langle \nu_\theta \rangle_\parallel$ increases strongly in the experiments with higher mean charge state $\langle Z\rangle$. Overall, the $\langle \nu_\theta \rangle_\parallel$ from collisions with ions can be seen to agree reasonably well with much of the data, while the $\langle \nu_\theta \rangle_\parallel$ from electron scattering tends to be ~10 × too small, at least at intermediate $\langle Z\rangle$. Since $\nu_{\theta,i} = \langle Z\rangle \nu_{\theta,e}$, the slopes of the two theory curves are different in Fig. 10, with the electron collisions actually appearing to have a slope closer to the data. Separating the effect of ion and electron scattering terms cleanly from trends in the data, however, is challenging due to the large scatter in the data and also the fact that increasing impurity charge state results in an increase in both ion rates (from increased nuclear charge) and electron rates (from additional bound electrons), with the curves only diverging linearly with $\langle Z\rangle$. The $\langle \nu_\theta \rangle_\parallel$ from synchrotron damping is typically a factor of ~ 10^3 too small to match the measurements, indicating that synchrotron damping is not affecting the current dissipation significantly in these experiments.

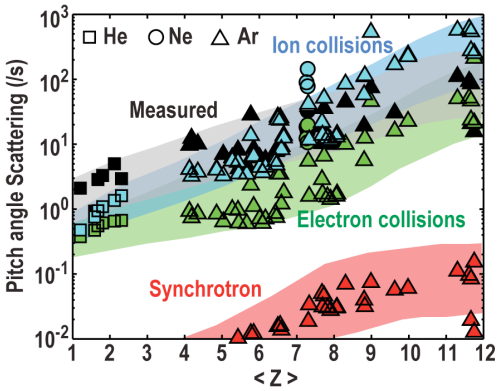

5. Discussion

The data presented here suggest that the anomalously fast (~10 × faster than avalanche theory) current dissipation typically observed in these experiments originates

from pitch angle scattering by impurity ions. As shown by Fig. 5(d), the current in the RE plateau tends to be carried by relativistic electrons with energy of order several MeV. These experiments therefore tend to fall in an intermediate energy regime with normalized momentum $1 < p < (1+\langle Z \rangle)$, where pitch angle scattering can be expected to have a strong effect on current dissipation [20]. In Figure 9, despite the large scatter in the data, there may be an indication that electron scattering becomes significant for current dissipation at very high and very low $\langle Z \rangle$. This might be consistent with $p \sim 1$ for very high $\langle Z \rangle$ and then $p > 1+\langle Z \rangle$ at very low $\langle Z \rangle$.

Another interesting finding of this work is that synchrotron damping does not appear to play a significant role in the energy dissipation of RE beams except perhaps in the lowest $\langle Z \rangle$ cases. However, it is possible that synchrotron damping is limiting the peak RE energy here. As mentioned in the introduction, the highest energy electrons will tend to cause deeper wall damage, so the distribution function of REs, (not just total energy) is important for predicting wall damage. As shown in Fig. 5(a), f_ε tends to fall off much faster at higher e than predicted by avalanche theory. Simple estimates of the observed peak energy are consistent with the peak energy being limited by either synchrotron damping or drift orbit losses. An example of this is shown in Fig. 11, where peak energy is plotted as a function of time for a long RE plateau without MGI. The measured "peak energy" is defined for the purposes of Fig. 11 as the energy in the reconstructed f_ε at which only a fraction 10^{-5} of the REs have a higher energy; this does a reasonable job of representing the steeper slope region after the knee in the distribution function at high energy. The synchrotron limit on RE energy can be estimated to be roughly $\gamma_{\max}^2 \approx \frac{6\pi\varepsilon_0 \rho_{ec}^2 E}{e\theta^2}$ [22], shown as the red curve in Fig. 11. For drift orbit losses to the wall, the peak energy can be estimated to be roughly $\gamma_{\max} \approx \left(\frac{R}{\rho_{ec}}\right)\frac{\mu_0 I_p}{2\pi a B_\phi}$ [22], shown by the blue curve in Fig. 11. The collision drag energy limit is defined as $ecE = F_D(\gamma_{\max})$, where F_D is the total collisional drag force on the REs by collisions with background electrons and ions as a function of RE energy; this is shown by the magenta curve in Fig. 11. Finally, the green curve in Fig. 11 shows the upper limit of RE energy in the absence of any drag forces, i.e. the energy obtained by

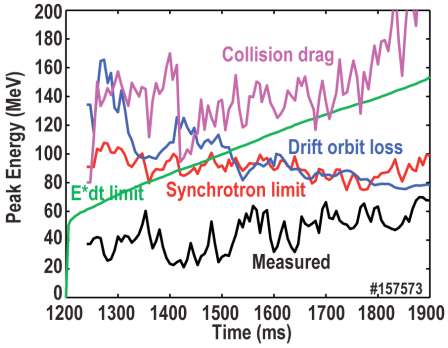

Fig. 11. Peak measured RE energy as a function of time compared with different estimates of limits on peak energy.

integrating the electric field with time: $d\gamma/dt = \left(eE/m_e c\right)\sqrt{1-1/\gamma^2}$. Overall, it can be seen that measured peak energy is closest to the synchrotron or drift orbit limits, especially later in the shot.

6. Summary

First attempts were made to reconstruct the RE energy distribution function during MGI into the RE plateau. Overall, f_ε is found to be more skewed toward low energy than predicted by avalanche theory. The reconstructions indicate that the RE pitch angle θ is not uniform, but tends to be large at low energies and small (θ ~ 0.1 - 0.2) at high energies. Overall power loss from the RE plateau appears to be dominated by collisions with background electrons, leading to line radiation. The influence of pitch angle scattering off impurity ions appears to be important for dissipating plasma current (and magnetic energy). Synchrotron emission appears not to be significant for overall energy dissipation, but may be important for limiting the peak RE energy. Further work will be necessary to allow predictions of the optimum MGI mix and quantity to use for RE plateau mitigation in ITER. In particular, the RE-wall interaction is expected to cause a large rise in loop voltage and significantly change the distribution function from the centered plateau value. Additionally, very little is known at present about the RE-wall strike area or timescale and how these are affected by the RE plateau composition.

References

[1] T. Feher, H.M. Smith, T. Fulop, and K. Gal, Plasma Phys. Control. Fusion 53, 035014 (2011)

[2] Z.Y. Chen, W.C. Kim, Y.W. Yu, A.C. England, J.W. Yoo, S.H. Hahn, S.W. Yoon, K.D. Lee, Y.K. Oh, J.G. Kwak, and M. Kwon, Plasma Phys. Control. Fusion **55**, 035007 (2013)

[3] R. Nygren, et al J. Nucl. Mater. **241**, 522 (1997)

[4] T.C. Hender, et al Progress in the ITER physics basis: Chapter 3. MHD stability, operational limits, and disruptions, Nucl. Fusion **47**, S128 (2007)

[5] V. Sizyuk, et al., Nucl. Fusion **49**, 095003 (2009)

[6] E.M. Hollmann, et al., "Status of research toward the ITER disruption mitigation system," Phys. Plasmas, accepted (2014)

[7] R. Yoshino and S. Tokuda, Nucl. Fusion **40**, 1293 (2000)

[8] M. Lehnen, et al., Phys. Rev. Lett. **100**, 255003 (2008)

[9] N. Commaux, et al., Nucl. Fusion **51**, 103001 (2011)

[10] V. Riccardo, Fus. Sci. Tech. **53**, 1064 (2008)

[11] G. Papp, M. Drevlak, T. Fulop, and G.I. Pokol, Plasma Phys. Control. Fusion **54**, 125008 (2012)

[12] E.M. Hollmann, et al., Nucl. Fusion **53**, 083004 (2013)

[13] F. Saint-Laurent, G. Martin, T. Alarcon, A. Le Luyer, P.B. Parks, P. Pastor, S. Putvinski, J. Bucalossi, S. Bremond, and Ph. Moreau, Fusion Sci. Tech. **64**, 1 (2013)

[14] J.R. Martin-Solis, A. Loarte, E.M. Hollmann, B. Esposito, V. Riccardo, FTU and DIII-D Teams and JET EFDA Contributors, Nucl. Fusion **54**, 0832027 (2014)

[15] J.L Luxon, Nucl. Fusion **42**, 614 (2002)

[16] M.N. Rosenbluth and S.V. Putsinski, Nucl. Fusion **37**, 1355 (1997)

[17] P.B. Parks, M.N. Rosenbluth, and S.V. Putvinski, Phys. Plasmas **6**, 2523 (1999)

[18] D.A. Humphreys, et al., Phys. Plasmas **13**, 056113 (2006)

[19] E.M. Hollmann, P.B. Parks, D.A. Humphreys, N.H. Brooks, N. Commaux, N. Eidietis, T.E. Evans, R. Isler, A.N. James, T.C. Jernigan, J. Munoz, E.J. Strait, C. Tsui, J. Wesley, and J.H. Yu, Nucl. Fusion **51**, 103026 (2011)

[20] G. Fussmann, Nucl. Fusion **19**, 327 (1979)

[21] F. Andersson, P. Helander, and L.G. Eriksson, Phys. Plasmas 8, 5221 (2001)

[22] I. Entrop, "Confinement of relativistic runaway electrons in tokamak plasmas," (PhD Thesis, Technical University of Eindhoven, 1999)

Acknowledgements

This material is based upon work supported by the U.S. Department of Energy, Office of Science, Office of Fusion Energy Sciences, using the DIII-D National Fusion Facility, a DOE Office of Science user facility, under Awards DE-FG02-07ER54917, DE-FG03-97ER54415, DE-FC02-04ER54698, DE-AC05-00OR22725, DE-AC52-07NA27344, and DE-AC05-06OR23100. DIII-D data shown in this paper can be obtained in digital format by following the links at https://fusion.gat.com/global/D3D_DMP.

The maintenance and operation of diagnostics by J. Kulchar, D. Ayala, M. Van Zeeland, A. Briesemeister, D. Kaplan, T. Leonard, Z. Unterberg, M. Schaffer, and D. Thomas is gratefully acknowledged.